Laser Photochemistry of Molecular Oxygen

DAVID H. PARKER
Department of Molecular and Laser Physics, University of Nijmegen, Toernooiveld 1, 6525 ED Nijmegen, The Netherlands

Received February 4, 2000

ABSTRACT
Molecular oxygen poses very difficult challenges in molecular photochemistry due to the extreme weakness of its ultraviolet absorption spectrum. In the past few years a new technique called velocity map imaging has been able to overcome many of the experimental obstacles to the study of this all-important atmospheric species. In this Account several aspects of laser photochemistry of O_2 will be described, including the unraveling of the Herzberg and Schumann−Runge continua using velocity map imaging.

I. Introduction

Molecular oxygen dominates atmospheric chemistry as completely as it challenges the spectroscopists and chemists who study it. Its dominant role comes from the great abundance, reactivity, and photosensitivity of O_2 in the atmosphere. Molecular nitrogen, in comparison, is more abundant but chemically inert and essentially transparent to solar radiation. The challenge of O_2 arises from its electronic structure, which determines all of its photochemical properties such as the optical absorption strength and fragmentation products. Not only is the O_2 electronic structure very complex, it is also difficult to probe by standard optical spectroscopy due to the strict symmetry selection rules applicable to homonuclear diatomic molecules. In the past few years, experimental techniques have become available to study a number of "real-world" problems involving molecular oxygen. Our research focuses on the first step in O_2 photochemistry, photodissociation by ultraviolet light. We hope to contribute to a fully quantitative understanding of the absorption process and its consequence at all relevant wavelengths. With this information, highly accurate modeling of O_2 photochemistry under all conditions in the atmosphere should be possible.

Intense lasers and fast electronics have made the new studies in photodissociation possible. Intense lasers, however, create their own extra complications in experimental investigation of O_2 photochemistry, especially when probing the spectral regions where the molecule shows extremely weak absorption. As will be described in this Account, velocity map imaging,[1] a two-dimensional imaging technique introduced by our group in 1997, is now able to sort out the many different signals arising from "normal" one-photon absorption and laser-induced multiple photon absorption by O_2. Velocity map imaging is an extension of the ion imaging technique introduced by Chandler and Houston in 1987.[2] It has important advantages in several areas of experimental chemistry, including photodissociation,[3] photoionization,[4] and bimolecular scattering.[5] In this Account, studies from our laboratory[6−9] using velocity map imaging on the laser photochemistry of O_2 are described, and an outlook to the future of the field is given.

II. Solar and Laser-Driven Molecular Oxygen Photochemistry

UV Absorption by Molecular Oxygen. Photochemistry begins with photodissociation, and O_2 photodissociation is very dependent on the wavelength of the absorbed light. For O_2, three different wavelength regions where dissociation takes place can be specified: 242−200 nm (the Herzberg continuum), 200−176 nm (the Schumann−Runge bands), and 176−100 nm (the Schumann−Runge continuum). At energies below the Herzberg continuum lie the Herzberg bands, which do not lead to dissociation. These regions and their absorption strength and dissociation products are shown schematically in Figure 1.

A typical absorption cross section, σ, for an allowed transition is 10^{-17}−10^{-18} cm^2. Ozone, for example, has a peak absorption at 260 nm of $\sigma \approx 10^{-17}$ cm^2. As can be seen in Figure 1a, absorption by O_2 at 260 nm is 8 orders of magnitude weaker than that by ozone, but σ does increase progressively at shorter wavelengths to peak at $\sim 10^{-17}$ cm^2 in the vacuum UV (VUV) around 130 nm. In general, the absorption spectrum of a diatomic molecule is sharply structured, broad-banded, or a continuum. The Herzberg bands are sharply structured, indicating a *stable* excited electronic state, while the Schumann−Runge bands are structured but broadened, indicating that the excited $B^3\Sigma_u^-$ state is coupled indirectly to the first dissociation continuum in a process called *predissociation*, producing two $O(^3P)$ atoms. The Herzberg and Schumann−Runge continua indicate a *directly dissociative* excited electronic state, yielding $O(^3P) + O(^3P)$ and $O(^3P) + O(^1D)$ products, respectively.

Potential energy curves for several excited electronic states of O_2 are shown schematically in Figure 1b. The six strongly bound states originating from ground-state ($O(^3P)$) atoms are unique in that there are no optically allowed transitions among them. Selection rules restrict excitation from the electronic ground state to upper states of $^3\Sigma_u^-$ and $^3\Pi_u$ symmetry. The three upper excited electronic states $c^1\Sigma_u^+$, $A'^3\Delta_u$, and $A^3\Sigma_u^+$ are known collectively as the

David H. Parker was born on the Fourth of July, 1953, in Camden, South Carolina. He received his B.A. at the University of California at Irvine and his Ph.D. in 1979 in physical chemistry from the University of California at Los Angeles in the group of Prof. Mostafa El-Sayed. His thesis was one of the earlier studies of resonance-enhanced multiphoton ionization in polyatomic molecules. Postdoctoral work with Prof. Richard Bernstein at Columbia University centered on the crossed-beam reactive scattering of oriented molecules. After serving as an Assistant and Associate Professor at the University of California at Santa Cruz, he joined the Department of Laser and Molecular Physics at the University of Nijmegen in 1990 as a professor of physics. His research interests include the study of molecular photodissociation, photoionization, and reaction dynamics and the development and application of ultrasensitive laser methods for trace gas analysis.

10.1021/ar980012d CCC: $19.00
Published on Web 07/28/2000

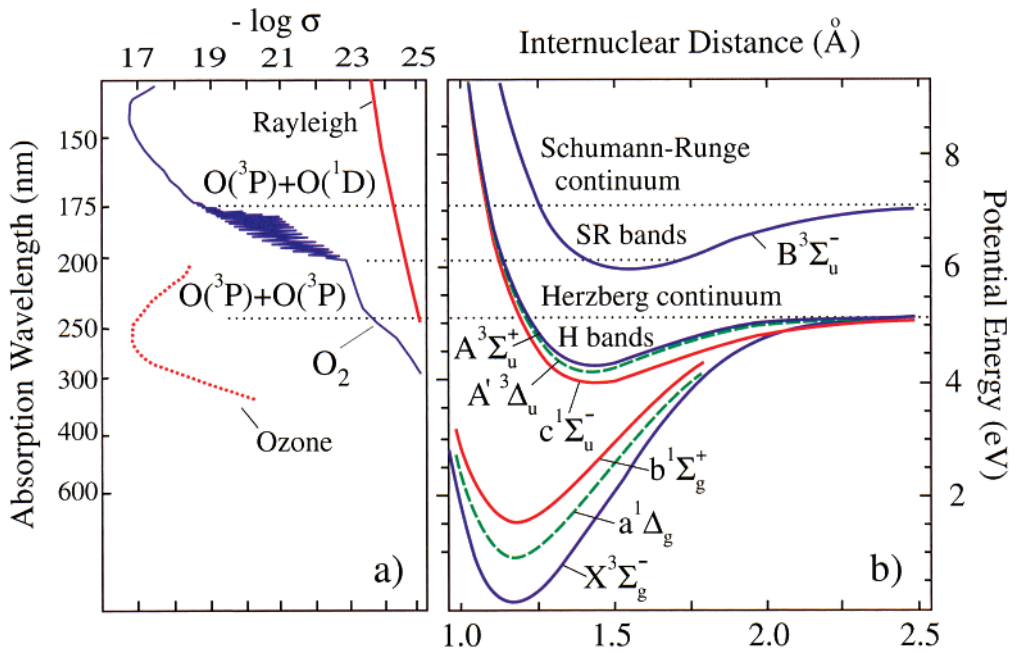

FIGURE 1. Absorption spectrum and potential energy curves for O_2 in the UV−VUV region. Note the logarithmic scale for absorption on the upper left panel of the figure. Cross sections (cm^2) for Rayleigh scattering and ozone absorption are also included in this panel. The first ($O^3P + O^3P$) and second ($O^3P + O^1D$) dissociation limits are indicated at 242 and 176 nm, respectively. The optimal region for Franck−Condon overlap is shown as a shaded vertical stripe around 1.2 Å in the right panel of the figure.

Herzberg states. Although transitions to these states are optically forbidden, they gain a small amount of absorption strength due to spin−orbit and spin−rotation coupling with optically allowed electronic states lying at higher energy. Transitions to the Herzberg states appear as very weak, narrow-line bands between 270 and 242 nm and a broad, weak continuum between 242 and ~180 nm. Franck−Condon overlap determines the spectral envelope of these transitions. As can be seen in Figure 1b, the ground state overlaps optimally with the unbound parts of the potential energy curves of the Herzberg states and also the higher-lying electronically excited $B^3\Sigma_u^-$ state, causing the absorption curve to peak in the continuum. Optical excitation is fully allowed to the $B^3\Sigma_u^-$ state and results in the Schumann−Runge transition between ~200 and 100 nm.

Formation of the Ozone Layer. Sunlight converts O_2 to O_3, forming the ozone layer. While ozone photochemistry is one of the few chemical processes known to the general public, many of the details are uncertain and often surprising. For example, the first step in the ozone-making process, photodissociation of O_2 by ultraviolet (UV) solar radiation to two ground-state O atoms, is distinctive in its high improbability, occurring for a single O_2 molecule only once in about 1500 years! Ozone is formed in the *Chapman Layer* in a reaction sequence given by

$$O_2 + h\nu\ (242 < \lambda < 176\ \text{nm}) \rightarrow O(^3P) + O(^3P) \quad (1a)$$

$$O(^3P) + O_2 + M\ (M = O_2, N_2) \rightarrow O_3 + M \quad (1b)$$

With increasing altitude the O_2 density decreases exponentially while the UV intensity increases exponentially. The primary process in ozone formation is O_2 photodissociation by UV radiation, and the efficiency of this process is thus a product of O_2 density and UV intensity. This product exhibits a maximum at 25 km. Even though the cross sections for the Herzberg transitions are only 10^{-23}−10^{-24} cm^2, these transitions lead to not less than 90% of the O_2 photodissociation in the lower stratosphere (overhead sun). This is illustrated by the results of simple rate model calculations[10] based on solar radiation at a blackbody temperature of 4945 K (realistic for the upper atmosphere). Combining the wavelength- and altitude-dependent solar flux $I(\lambda)$ and absorption cross section $\sigma(\lambda)$ yields an integrated rate coefficient $I\sigma$ of only $\sim 2 \times 10^{-11}$ s^{-1}. Multiplying by the O_2 density yields the altitude-dependent rates shown in Figure 2. At 25 km this product is still sufficiently large to result in a peak photodissociation rate of 2×10^6 cm^{-3} s^{-1}. This rate produces the overhead ozone concentration in a time interval of less than a few weeks, and at the stratopause level (~35−40 km) even within 6 h. While the rate coefficient keeps increasing with altitude, the rate of O_2 dissociation diminishes due to the lowering O_2 density. Around 50 km, the role of the Herzberg continuum is taken over by the Schumann−Runge band system. Absorption due to the Schumann−Runge continuum is so strong that essentially all radiation of wavelength less than 170 nm is blocked below 120 km. The ozone layer thus exists only because the Herzberg continuum is so weak, i.e., the small absorption cross section allows radiation to penetrate to depths in the atmosphere where the O_2 concentration is sufficient for the reaction sequence of eq 1 to take place.

Laser Photochemistry and the Herzberg Continuum. For general principles and for modeling the photochemistry of the atmosphere, a good understanding of the

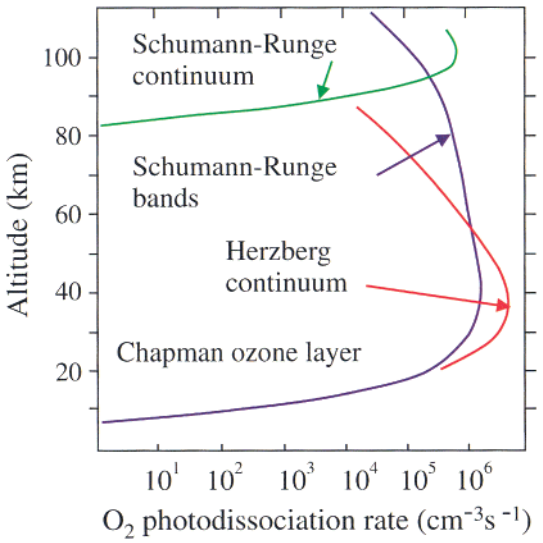

FIGURE 2. Photodissociation rates for O_2 in the atmosphere due to the different regions of the O_2 absorption spectrum labeled in Figure 1. The wavelength dependence of each region is combined with the altitude-dependent solar spectral curve and integrated over 500 cm^{-1} steps. Below 20 km the Herzberg continuum and Schumann–Runge bands yield similar rates. Between 20 and 50 km the Herzberg continuum accounts for the largest fraction of dissociation.

strength and coupling mechanisms resulting in the Herzberg continuum of O_2 is important. This is quite challenging because the coupling mechanisms depend on the O_2 rotational quantum states populated and thus on the temperature, which is altitude dependent. Furthermore, absorption can also be collision induced and thus pressure dependent, which is known to be the case especially for the $c^1\Sigma_u^-$ state. Many different experimental and theoretical studies have been carried out to better understand the Herzberg continuum. Our efforts are focused on the *optical signature* of the overall transition. The goal is to determine how much each of the three Herzberg states contributes to the total absorption under experimental conditions where the rotational temperature and wavelength are well defined.

The weak absorption strength of the Herzberg continuum makes laboratory studies using conventional light sources almost impossible. Lasers provide sufficient photon flux to excite O_2 in this spectral region, but the high flux needed for normal one-photon excitation makes two-photon and higher-order excitation likely. Laser and sunlight excitation can be qualitatively compared using simple rate equations. For solar-driven processes the Herzberg continuum excitation frequency at 25 km is estimated to be $\sim 2 \times 10^{-11}$ s^{-1}, assuming a solar flux of $I \approx 2 \times 10^{13}$ photons cm^{-2} s^{-1} and an absorption cross section $\sigma = 1 \times 10^{-24}$ cm^2. In a laboratory experiment using a typical laser pulse length of $\Delta t = 5$ ns, excitation with a probability P of $\sim 10^{-7}$ is detectable, where $P = \sigma I \Delta t$. This is possible with an instantaneous laser flux of 2×10^{25} photons cm^{-2} s^{-1}. Modern pulsed tunable lasers can easily achieve this flux when focused, and unlike solar radiation, their wavelength spread is less than 2×10^{-5} or 1 cm^{-1} at 50 000 cm^{-1} (200 nm). The problem is that a typical two-photon absorption cross section $\sigma^{(2)}$ is around 10^{-50} cm^4 photon^{-2} s^{-1} which, assuming the above conditions, yields a probability for two-photon absorption $P^{(2)} = \sigma^{(2)} I^2 \Delta t = 2 \times 10^{-8}$. Two-photon absorption is thus almost as probable as one-photon absorption, and resonance-enhanced three-photon absorption is also quite likely. Multiphoton excitation for discrete transitions is also enhanced by the narrow bandwidth of the laser. The study of highly forbidden states such as the Herzberg states is therefore complicated by the possibility of many other higher-order processes.

Fragment Angular Distributions: The Optical Signature of Absorption. Direct dissociation of a diatomic molecule occurs along the bond axis within one vibrational period, well before the molecule has a chance to rotate. Optical excitation of a randomly oriented sample of molecules with linearly polarized light favors those molecules whose bond axis lies parallel to the polarization direction of the light, if the transition moment lies along the bond axis (parallel transition, $\Delta\Omega = 0$), or it favors molecular bonds lying perpendicular to the polarization direction for a perpendicular transition ($\Delta\Omega = 1$). The fragment atoms will either fly off parallel or perpendicular to the polarization direction of the light field. For normal optical excitation the angular distribution of the ejected fragments is given by

$$S(\theta) = (1 + \beta P_2(\cos\theta))/4\pi \qquad (2)$$

with θ the angle between the fragment velocity vector and light polarization direction, and $P_2(\cos\theta)$ the second Legendre polynomial. β in this expression is equal to 2 for a parallel transition and -1 for a perpendicular transition. In the case of mixed absorption such as the Herzberg continuum, β lies between the two extremes. By measuring the angular distribution of the fragments the percentage of parallel versus perpendicular character can be determined.

Predissociation, as in the Schumann–Runge bands, is not instantaneous. Should the molecule rotate before dissociation, the degree of correlation between the electric field vector of the light and the fragment recoil direction will be lowered, but not completely to zero. For predissociation when the lifetime τ of the excited state is similar to the parent molecule rotational period T (and the according rotational frequency $\nu = 1/T$ of that state), the anisotropy parameter is given in the classical (high J) limit by

$$\beta_{\parallel}(\tau) = 2(\nu^2\tau^2 + 1)/(4\nu^2\tau^2 + 1) \qquad (3)$$

for a parallel transition, and

$$\beta_{\perp}(\tau) = -(\nu^2\tau^2 + 1)/(4\nu^2\tau^2 + 1) \qquad (4)$$

for a perpendicular transition. The limiting values for these anisotropy parameters are $\beta_{\parallel} = 0.5$ and $\beta_{\perp} = -0.25$. Measurement of β for each final product channel thus provides information on the symmetry of the electronic states involved in the absorption process and the lifetime of a single state with respect to rotation.

When there are multiple fragmentation pathways, each channel has a unique kinetic energy release given by

$$\mathrm{KER} = nh\nu - D_o - E_{A\,int} - E_{B\,int} \qquad (5)$$

where n is the number of photons absorbed, D_o is the bond dissociation energy (5.1145 eV), and $E_{A(B)\,int}$ is the internal energy of atom A(B) (1.967 eV for $O(^1D)$, 4.23 eV for $O(^1S)$). When $n > 1$, the angular distribution can be much more complicated than the simple $\cos^2\theta$ or $\sin^2\theta$ of eq 2. The experiment involves dissociation of the O_2 molecule with tunable laser light between 242 and 180 nm (for the Herzberg continuum), identification of each n-photon dissociation process by its kinetic energy release, and measurment of the angular distribution for the one-photon dissociation process. More than 20 dissociation channels are accessible at the energy sum of three 200 nm photons; thus, relatively high kinetic energy resolution is needed to distinguish the O atom signals arising from multiphoton excitation.

Detailed Dynamical Information from Photodissociation Imaging. From the product angular distribution, the symmetry of the optically excited electronic state of the parent molecule can usually be identified. Even more can be learned about the dynamics and mechanisms of photodissociation from the dependence of the image on the polarization of the detection laser. Wigner and Witmer showed many years ago that molecular electronic states could be constructed from the separated atomic orbital limits using molecular orbital theory.[11] Construction of the lower electronic states of O_2 begins with two $O(^3P_J)$ atoms with $J = L + S$, $L = 1$, $S = 1$, $M_L = 1,0,-1$, $M_S = 1,0,-1$, where the molecular axis defines the projection of L and S. Using the correlation diagram method of Wigner and Witmer is possible but complicated, as shown by Slater,[12] because the molecular orbitals must be combined from the atomic orbital basis states in the proper combinations that satisfy all of the constraints arising from the many symmetry elements of a homonuclear molecule. For the Herzberg states the only direct conclusion about the final product quantum numbers is that the final $O(^3P_J)$ atoms must be formed in the lowest-energy $J = 2$ state. In the case of the upper state of the Schumann−Runge bands, the $B^3\Sigma_g^-$ state, the atomic orbital parentage is more clear: the electronic state must fall apart into an $O(^3P)$ atom plus an $O(^1D)$ atom with $M_J = 0$; i.e., the valence electron orbital of the $O(^1D)$ atom is *aligned* perpendicular to the molecular axis. Ionization of an aligned atom will affect the appearance of the velocity map image. The Wigner−Witmer correlations are defined in the so-called zero-order limit, where weaker types of angular momentum coupling such as orbit−rotation coupling are ignored. If different final state products are observed, a curve-crossing mechanism for coupling the initial excited electronic state with other electronic states is in effect. These are the rich details of the properties of molecules that can be directly confirmed with our most advanced quantum mechanical theories. The basic principles outlined above have been known for many decades, but experiments that directly probe all of the possible quantum states of the final products have only recently become possible. Imaging techniques such as velocity map imaging are particularly powerful for this purpose because the experiment simultaneously measures the product state quantum state distribution and recoil (bond axis) direction (a so-called vector correlation). This will be illustrated in the following section on dissociation in the Schumann−Runge continuum.

III. How Velocity Map Imaging Works

As scientists are usually quite fond of explosions, taking a picture of an exploding molecule must have been an early dream of many photochemists. Solomon[13] was the first to realize this dream in 1967, directly in three dimensions, using photochemical etching inside a glass hemisphere to capture the angular distribution of I atoms from the photodissociation of I_2 by polarized light. In 1987 Chandler and Houston introduced ion imaging,[2] the basis of the method described here. Ion imaging provides quantitative kinetic energy release data and uses laser ionization, a very general detection method, but it did not provide sufficient image resolution. Our contribution was to introduce a special electrostatic lens that dramatically improves the ion image resolution by a factor of at least 20. Energy resolution equivalent to vibrational and in some cases rotational spacing in molecules[14] is now readily achieved.

Photofragment imaging works as follows. Photodissociation of a single O_2 molecule yields two $O(^3P)$ atoms with equal speed flying in opposite directions in the center-of-mass frame. Under the same initial conditions a second O_2 molecule will produce a pair of fragments flying in a slightly different direction (depending on its initial orientation before absorption) but with the same speed. Each repeating fragment pair lies thus on the same expanding three-dimensional sphere as the first. This product velocity sphere is called a Newton sphere in molecular dynamics vernacular. After the process is repeated several thousand times, the Newton sphere develops with a fixed expansion velocity and a characteristic intensity pattern on its surface. It should be noted that Newton spheres describe all two-body processes including photodissociation, photoionization, and bimolecular events such as inelastic scattering and chemical reactions. A sensitive experimental technique for characterizing Newton spheres is useful in all branches of molecular dynamics.

A single Newton sphere is shown schematically in Figure 3 for a parallel dissociation process, where the laser polarization direction lies on the vertical axis of the figure. The fragments fly primarily along this direction, with a $\cos^2\theta$ distribution ($\beta = 2$ in eq 2). To detect the Newton sphere it is most convenient to convert the neutral particles into ions just as they are formed. This can be done with a second short-pulse laser tuned to resonantly excite and ionize the $O(^3P_J)$ atom in a resonance-enhanced multiphoton ionization (REMPI) process. Ionization barely

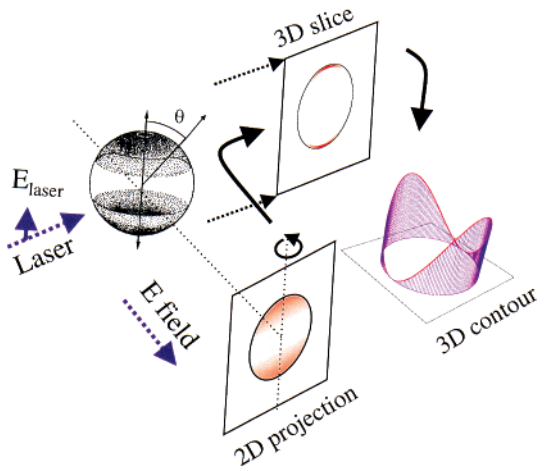

FIGURE 3. Measurement and analysis of a Newton sphere. The Newton sphere (left) is created using a linearly polarized laser with the polarization axis lying in the vertical direction of the figure. Fragment atomic ions are ejected with a fixed velocity primarily along this direction. An electric field projects the sphere of ions onto a two-dimensional detector (bottom). A mathematical inversion procedure recovers the 3D sphere. A slice through the sphere (top) shows the particle velocity and angular distribution. This information is also displayed as a 3D contour diagram (right side of figure).

changes the momentum of the parent atom; thus, the ion continues on with the same initial velocity of the neutral species. A very important advantage of ionization by a second laser is that it can be done fully state selectively, including the magnetic (directional) quantum number, for many target atoms by a suitable choice of the laser wavelength and polarization. Once the Newton sphere is converted to ions, it can be crushed in one direction onto a two-dimensional ion-sensitive detector such as a multichannel plate/phosphor screen device by a strong electric field.

In Figure 3 the light pattern emitted by the phosphor screen is shown as a disk with most of the signal on the outside edge and at the poles. Because there is cylindrical symmetry along the laser polarization direction, the two-dimensional pattern on the detector can be inverted back to its original three-dimensional form by the Abel inversion[15] as illustrated in the figure. A slice through this three-dimensional form calculated from the measured two-dimensional data yields the sought-after angular distribution information. This slice can also be presented as a three-dimensional angular distribution graph as plotted in Figure 3.

The experimental realization of Figure 3 uses the velocity mapping apparatus diagrammed in Figure 4. Details about the velocity mapping technique are found in ref 1, and only the basic features are described here. First, the Newton spheres of state-selectively ionized fragments are created within the laser/molecular beam-crossing volume. A high electric field bias accelerates and flattens the sphere of ions onto the detector. The arrival time of the ions is proportional to the square root of their mass; thus, by turning the detector on at this time, the particles can be mass-selectively detected. Key to the

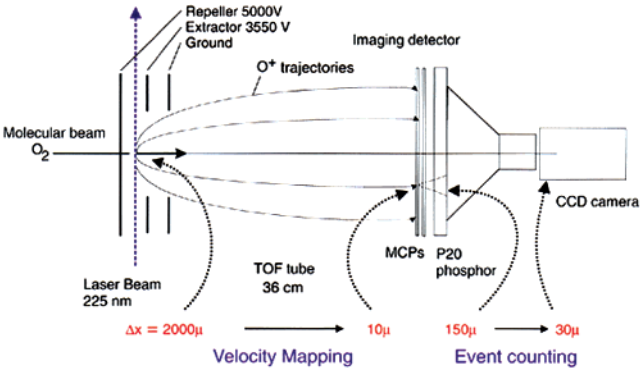

FIGURE 4. Apparatus diagram. Newton spheres such as the one shown in Figure 3 are created at the crossing of the laser and molecular beams. An open electrostatic lens assembly maps the particle velocities uniquely onto the detector, essentially independently of the spread ($\Delta x = 2$ mm) in the initial ionization position. A CCD camera with event counting software monitors the detector.

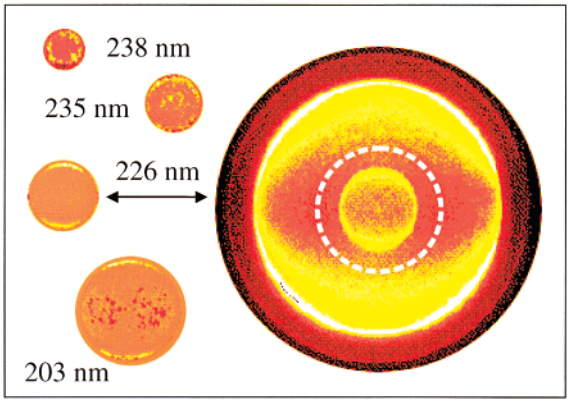

FIGURE 5. Raw images of $O(^3P_1)$ atoms from the photodissociation of O_2 at several wavelengths in the Herzberg continuum. A full image for dissociation at 226 nm is shown in which the Herzberg continuum signal is enclosed by a dashed circle. The image radius is proportional to velocity. Within the image disk a lighter color corresponds to higher signal levels. Laser polarization is in the vertical direction.

whole process is the electrostatic lens. When set correctly, the spread in origins of the Newton spheres formed is compensated to within the distance of the channel spacing of the multichannel plate detector. A CCD camera monitors the flashes of light on the back end of the detector. With the fast computers now available the center of each spot of light (event) is individually recorded for each laser pulse. The final image resolution is quite good, as illustrated in the following sections, and the apparatus works just as well for positive as for negatively charged species such as photoelectrons.

IV. Decomposition of the Herzberg Continuum

In a collaborative study[6] with research groups at AMOLF and Canberra, we have obtained and analyzed velocity map images of $O(^3P)$ atoms produced across the Herzberg continuum. A few sample images of $O(^3P_1)$ atoms are shown in Figure 5. Because the Herzberg states correlate with two ground-state $O(^3P_2)$ atoms, the observation of $O(^3P_{1,0})$ atoms indicates curve crossing. A full image is

shown at 226 nm; the other partial images shown are the lowest-velocity $O(^3P_1)$ signals. As the full image shows, at higher velocities very strong $O(^3P)$ signals due to two-photon photodissociation are observed. Previous Doppler profile measurements[16] at this wavelength were complicated by the two-photon signal. At the lowest excess energy the angular distribution of fragments from the Herzberg continuum is nearly isotropic, while at shorter wavelengths it becomes more anisotropic in the direction of positive β. The angular distribution of the one-photon signal can be described by eq 2.

Intensity-borrowing mechanisms involving optically allowed states of different symmetries lead to an overall transition in the Herzberg continuum of mixed parallel ($\Delta\Lambda = \Delta\Omega = 0$) and perpendicular ($\Delta\Lambda = \Delta\Omega = \pm 1$) character. By measuring the angular distribution and J-state yields of each product $O(^3P_J)$ atom at different wavelengths, the amount of mixing can be determined. It is not yet possible to obtain all three J-state signals at every dissociation wavelength. In this case the sudden limit model for the relative J-state product distributions of Freed and co-workers[17] is assumed. This allows the calculation of a fine-structured averaged β value. At 226 nm, for example, $\beta = 0.612$, implying that the dissociation has a 54% parallel character ($\beta = 2$) and a 46% perpendicular character ($\beta = -1$). A very extensive analysis of the latest theoretical and experimental basis set of O_2 absorption cross sections, potential energy curves, R-dependent transition moments, and perpendicular−parallel transition character has been presented.[6] This analysis allows a direct prediction of $\beta(\lambda)$ from theory. For dissociation at 226 and 204 nm the agreement of theory with the fine-structure weighted experimental values is within 10%. More details on the direct comparison of theory with the velocity mapping data are given in ref 6. When this information is combined with the considerable knowledge of the intensity-borrowing mechanisms in O_2, the individual contributions of the $A^3\Sigma_u^+$, $c^1\Sigma_u^-$, and $A'^3\Delta_u$ states respectively can be extracted. Results are presented schematically in Figure 6, which shows that the $A^3\Sigma_u^+$ state is the dominant contributor to the Herzberg continuum. Overlap with the much stronger Schumann−Runge bands (next section) complicates analysis of the short-wavelength side of the Herzberg continuum.

The observation of $O(^3P_{1,0})$ atoms indicates that curve crossing takes place during the photodissociation process. Photodissociation dynamics can be characterized by an adiabaticity parameter[18] $\epsilon = \Delta R \Delta E_{SO}/h\nu$ which compares the recoil time $\Delta R/v$, where ΔR is a characteristic recoil distance and v is the recoil velocity, with the characteristic time for spin−orbit coupling. Two limiting cases, the sudden recoil limit and the adiabatic limit, correspond to high and low recoil velocity, respectively. In the sudden limit the atomic multiplet distribution is essentially statistical while in the fully adiabatic case Ω is conserved at all internuclear distances, and only $O(^3P_2)$ atoms are formed. O_2 photodissociation in the Herzberg continuum is intermediate, bordering on the statistical limit.

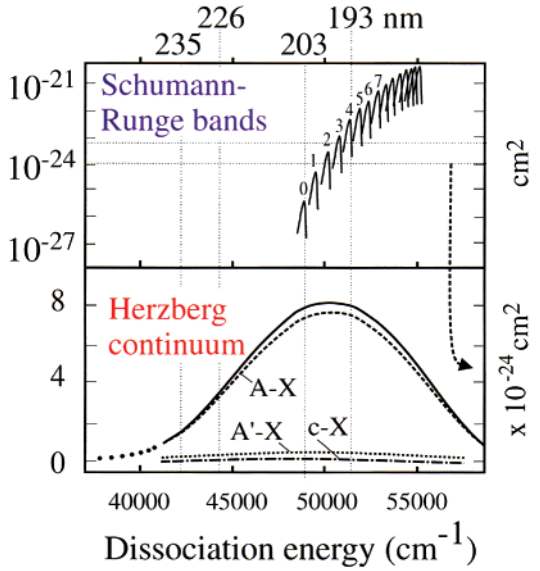

FIGURE 6. Absorption spectrum and decomposition of the Herzberg continuum of O_2. The upper panel shows the vibrational components of the Schumann−Runge bands, which overlap the Herzberg continuum beginning around 200 nm. The main dissociation wavelengths probed are indicated with dashed vertical lines. In the lower panel the total absorption and separate components of the three Herzberg states are shown. Note the difference in scales for the two panels.

V. Schumann−Runge Bands: Predissociation

Deeper into the VUV, the strong but predissociated bands of the Schumann−Runge system (205−130 nm) begin to overlap the Herzberg continuum (see Figures 1 and 6). These bands have been extensively studied previously using a wide range of experimental methods. Particularly relevant for predissociation dynamics are the coincidence experiments of Neumark and co-workers[19] in which the velocity distributions for all combinations of three final J states could be resolved.

Predissociation shortens the lifetime of the bound levels of the $B^3\Sigma^-_u$ state and results in the production of two $O(^3P)$ atoms. Our goal in this wavelength region is to extract more information on the Herzberg continuum after correcting for effects of the Schumann−Runge bands. We used a tunable ArF laser in either the tunable narrow-bandwidth ($\Delta E \approx 1$ cm^{-1}) or in the nontunable broad-band ($\Delta E \approx 200$ cm^{-1}) mode. In the narrow-band mode the laser can be selectively tuned on- and off-resonance with the $J = 15-23$ rotational states of the $B(v = 4) \leftarrow X(v = 0)$ Schumann−Runge bands. Using the ArF laser in the broad-band mode ($\Delta E \approx 200$ cm^{-1}) is a sensitive way to probe the Herzberg continuum.[9] Predissociation lifetimes of the $B^3\Sigma_u^-$ excited electronic state can be determined from the angular distribution anisotropy using eq 3, and these values are compared with previously measured rates from spectroscopic line widths.[20] In this study a tunable ArF laser was used to selectively excite a single rotational level in the $B^3\Sigma_u^-$ ($v = 4$) manifold. Figure 7 shows the angular distributions for the one-photon dissociation signal when resonant with a Schumann−Runge

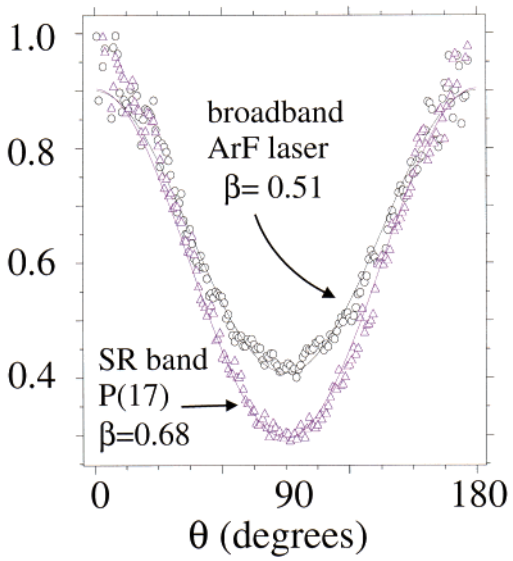

FIGURE 7. Analysis of predissociation in the Schumann−Runge bands of O_2. Angular distributions of $O(^3P_2)$ atoms created after excitation of the P(17) line in the ($v = 4$) manifold of the $B^3\Sigma_u^-$ excited electronic state are shown. Broad-band and narrow-band 193 nm light resonant with the P(17) line are compared.

band, in this case the P(17) transition at 51 736 cm^{-1}. Fitting to eq 2 yields $\beta = 0.68 \pm 0.05$. Correction for a broad-band component present in the laser output yields the experimental $\beta = 0.82 \pm 0.05$. Previous studies have determined the lifetime-broadened line width and rotational constants of the same upper state.[20] These values, when converted to state lifetime τ and rotational frequency ν, yield from eq 3 a value of $\beta = 0.78 \pm 0.02$, which is in good agreement with the corrected experimental value. Similar agreement is found for the other rotational states of the $B^3\Sigma^-_u$ ($v = 4$) manifold that lie within the tuning curve of the ArF laser. This and other studies have helped to build confidence in extracting quantitative information from velocity mapping angular distributions.

VI. Schumann−Runge Continuum: Product Atom Alignment

Photodissociation in the Schumann−Runge continuum requires a VUV photolysis source. Several studies on product state and angular distributions in this region have been reported using fluorine laser radiation at 157 nm.[18,21] An alternative means of accessing this energy region is to use a very intense visible laser to excite the optically forbidden metastable $b^1\Sigma_g^+$ state shown in Figure 1, and then photodissociate the b state with UV photons.[22] The same UV light also drives a REMPI detection process for $O(^3P)$ product atoms (at 226 nm, total $E = 7.12$ eV) or $O(^1D)$ product atoms (at 205 nm, total $E = 7.71$ eV). While the B−b excitation is dipole forbidden, a thorough theoretical analysis[23] has shown that the upper state is indeed the $B^3\Sigma_u^-$ state. An image of O^+ atoms produced in the excitation/detection scheme for $O(^1D)$ is shown in Figure 8. Both partners for the dissociation process have been measured and should, from conservation of momentum, show the same angular distribution, in this case a $\cos^2\theta$ pattern indicative of a $\Sigma-\Sigma$ transition. The $O(^3P_2)$ distribution is indeed $\cos^2\theta$, but the $O(^1D)$ distribution is unusual, showing a dip in signal along the vertical axis. This is due to the strong alignment ($M_J = 0$) of the $O(^1D)$ atoms, which is predicted for adiabatic dissociation by the correlation diagrams. The M_J distribution has been quantified and is shown to be 93% $M_J = 0$, 7% $M_J = \pm 2$, indicating that the dissociation process is remarkably adiabatic. These results also are consistent with the conclusions of a previous study of Huang and Gordon[18] at a slightly higher energy in the Schumann−Runge continuum.

VII. Analysis of REMPI in O_2: Multiphoton Excitation

REMPI (resonance-enhanced multiphoton ionization) is a standard means for detecting many types of molecules. REMPI of O_2 is complicated by the fact that along with

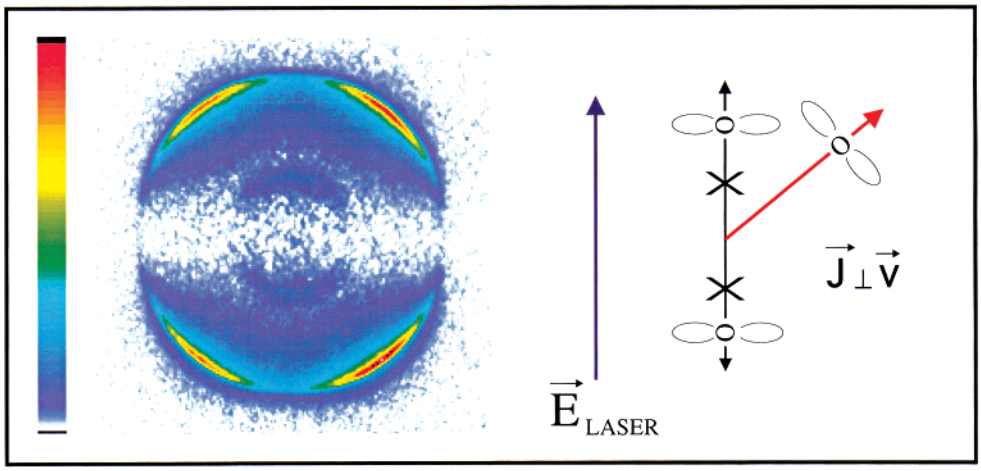

FIGURE 8. Raw image of $O(^1D)$ atoms from the photodissociation of O_2 in the Schumann−Runge continuum. The polarization direction of the dissociation and ionization laser is in the vertical direction. Due to the complete orbital alignment of the O (^1D) atoms ($M_J = 0$) the vertically moving atoms cannot be ionized by the vertically polarized laser beam. A weaker signal due to photodissociation of O_2^+ is seen in the middle of the image.

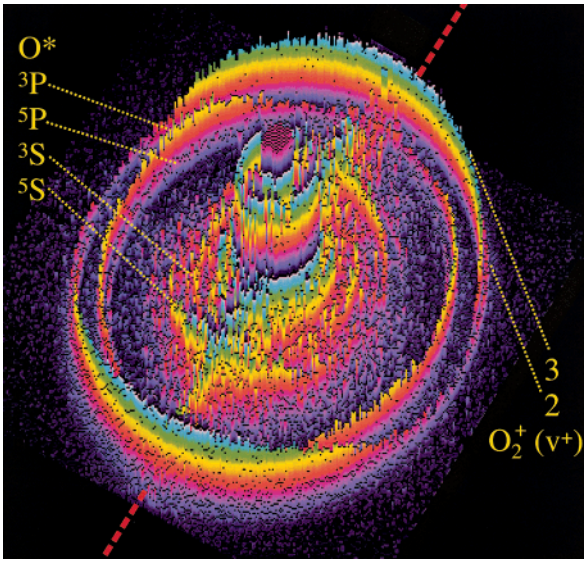

FIGURE 9. Photoelectron image from (2 + 1) REMPI of O_2 at 225.6 nm, shown as a 3D contour diagram. The laser polarization vector lies parallel to the striped diagonal line. Rings in the image are labeled for ionization of O_2, creating $O_2^+(v)$ in the $v = 2$ and 3 vibrational levels, and ionization of O atoms in the 3s(^{5}S,^{3}S) and 3p(^{5}P,^{3}P) electronically excited states.

O_2^+, a strong O^+ signal is often observed. Velocity mapping is a very powerful tool for analyzing the O^+ production process in that both the O^+ and the photoelectron angle−velocity distributions can be measured with equal sensitivity and resolution. An O^+ signal is present in almost all of our O_2 imaging studies, even when the laser used for REMPI of the O atom dissociation product is not present. An example is the small ring seen near the middle of Figure 8.

Three-photon absorption by O_2 (two-photon absorption below 200 nm) brings the molecule above the 12.08 eV ionization potential, making possible the formation of O_2^+ plus a photoelectron. Photons with energy >6.8 eV will photodissociate ground-state O_2^+ ion, creating the observed O^+ ions, ($O_2^+ \rightarrow O + O^+$), and lower-energy photons can dissociate vibrationally excited O_2^+ ions. Other processes producing O^+ after three-photon absorption include ion-pair formation ($O_2 \rightarrow O^- + O^+$), dissociation to electronically excited atoms ($O_2 \rightarrow O^* + O$) followed by one-photon ionization of the excited atom ($O^* \rightarrow O^+ + e^-$), and the three-body process dissociative ionization ($O_2 \rightarrow O + O^+ + e^-$). Depending on the three-photon energy, all of the above processes except ion-pair formation have been observed in the O^+ images. The small ring in Figure 8, for example, is due to dissociation by one 226 nm photon of $O_2^+(v = 3)$ formed by 226 nm two-photon absorption from the $b^1\Sigma_g^+$ state.

As an illustration of the power of velocity mapping in photoelectron spectroscopy consider Figure 9, a 3D contour plot of a photoelectron image created by (2 + 1) REMPI at 225.6 nm of O_2 in its ground electronic state. Figure 10 shows the kinetic energy distribution of the photoelectrons emitted perpendicular to the laser polarization. At least 20 different peaks are resolved in the image. The two-photon resonant state chosen is one of a

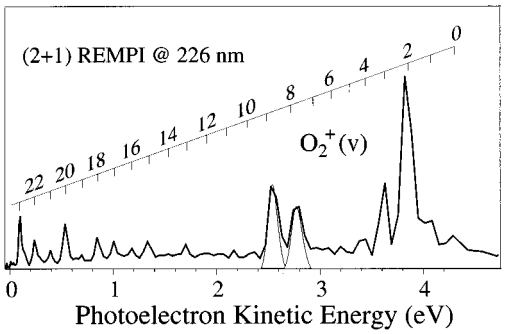

FIGURE 10. Kinetic energy distribution of photoelectrons produced by (2 + 1) REMPI of O_2 at 226 nm. This is a slice of the Abel-inverted image from Figure 9 for the electrons ejected perpendicular to the laser polarization vector. Two sets of signals are indicated: photoelectrons from the ionization of O_2 into vibrational levels labeled $v = 0$−24 of O_2^+, and photoelectrons from the ionization of electronically excited O atoms (shaded peaks). The raw image, which includes the full angular distribution information, for these data is shown in Figure 9.

large manifold of 4d,3s Rydberg states converging to the ground electronic state of O_2^+. A wide range of vibrationally excited $X^2\Pi_g$ O_2^+ ions is created by the REMPI process due to direct ionization and autoionization, and the angular distribution for electrons created in conjunction with each individual state can be obtained from the image. The photoelectron angular distribution probes the s,p,d... character and interference of the ejected photoelectron waves. The angular distributions vary widely with the O_2^+ vibrational level formed; for example, the distribution changes from negative β for $v = 2$ to positive β for $v = 3$. McKoy and co-workers[24] have predicted this sort of behavior previously using ab initio calculations and ascribed it to a so-called shape resonance effect. Ionization of 3s Rydberg O atoms yield positive β values (p-wave), while the 3p Rydbergs yields negative β values, indicating interference between s and d waves.

VIII. Future Directions

Much progress has been made in understanding the laser photochemistry of molecular oxygen due to recent advances in experimental methods. These methods will continue to develop and allow more quantitative measurements of product quantum state and angular distributions. What is needed are more accurate measurements of angular distribution parameters in the Herzberg continuum, along with similar studies using direct vacuum UV excitation in the Schumann−Runge continuum. Photodissociation of molecules excited to the long-lived metastable states of the Herzberg bands will also be of great interest in molecular oxygen photochemistry.

In terms of the velocity map imaging method, the kinetic energy resolution of the data shown in Figure 10 for velocity mapping of photoelectrons is also achievable for cations. Resolution scales with $(KE)^{1/2}$ and at 1 eV the apparatus resolution is at present ~25 meV. With larger detectors and further improvements in the electrostatic lens and molecular beams this resolution should eventu-

ally improve to ~2 meV, where rotational level spacing can also be routinely resolved.

The real power of velocity mapping is in its ability to correct for a large source volume. In photodissociation the source volume, defined by the laser−molecular beam crossing, is reasonably small, but in bimolecular studies such as inelastic and reactive scattering the source volume is defined by the crossing of two molecular beams and is thus much larger. Velocity mapping makes high-resolution imaging studies of crossed-beam scattering possible, a field which is just now beginning to flourish in several different laboratories across the world. Studies using unfocused synchrotron or free-electron laser radiation will benefit for the same reason. Finally, coincidence measurements using time-resolved imaging detection are also just beginning to show great potential. In these experiments the position and arrival time of correlated particles, e.g., electrons and parent ions, are recorded. Using femtosecond pump−probe techniques, intimate details of energy flow in molecules can now be charted.[25]

The Dutch National Science foundation and the European Union supported the work described in this Account. The research was carried out by a number of co-workers including Dr. Andre Eppink, Dr. Bart Buijsse, Dr. Ralph Delmdahl, Mr. Bernard Bakker, and Prof. Wim van der Zande, and a number of visitors to our laboratory.

References

(1) Eppink, A. T. J. B.; Parker, D. H. Velocity Map Imaging of Ions and Electrons using Electrostatic Lenses; Application in Photoelectron and Photofragment Ion Imaging of Molecular Oxygen. *Rev. Sci. Instrum.* **1997**, *68,* 3477−3484.

(2) Chandler, D. W.; Houston, P. L. Two-dimensional imaging of State-Selected Photodissociation Products by Multiphoton ionization, *J. Chem. Phys.* **1987**, *87*, 1445−1447.

(3) *Imaging in Chemical Dynamics*; Suits, A. G., Continetti, R. E., Eds.; ACS Symposium Series; American Chemical Society: Washington, DC, in press. See also: Chandler, D. W.; Parker, D. H. *Velocity Mapping Studies of Highly Excited Molecules*; Advances in Photochemistry 25; Wiley: New York, 1999; pp 59−106.

(4) Parker, D. H. Velocity Mapping Studies of Molecular Photodissociation and Photoionization Dynamics. *Photoionization and Photodetachment*; Advanced Series in Physical Chemistry 10A and 10B; World Scientific Publishing Co. Ltd.: Singapore, 2000.

(5) Yonekura, N.; Gebauer, C.; Kohguchi, H.; Suzuki, T. A crossed molecular beam apparatus using high-resolution ion imaging. *Rev. Sci. Instrum.* **1999**, *70*, 3265−3270. Lorenz, K. T.; Westley, M.; Chandler, D. W. Velocity map imaging of inelastic scattering processes. *Phys. Chem. Chem. Phys.* **2000**, *2*, 481−494.

(6) Buijsse, B.; van der Zande, W. J.; Eppink, A. T. J. B.; Parker, D. H.; Lewis, B. R.;. Gibson, S. T. Angular Distributions for photodissociation of O_2 in the Herzberg continuum. *J. Chem. Phys.* **1998**, *108,* 7229−7243.

(7) Eppink, A. T. J. B.; Buijsse, B.; Janssen, M. H. M.; van der Zande, W. J.; Parker, D. H. Production of maximally aligned $O(^1D)$ atoms from two-step photodissociation of molecular oxygen. *J. Chem. Phys.* **1998**, *108,* 1305−1308.

(8) Parker, D. H.; Eppink, A. T. J. B. Photoelectron and photofragment velocity map imaging of state-selected molecular oxygen dissociation/ionization dynamics. *J. Chem. Phys.* **1997**, *107*, 2357−2362.

(9) Bakker, B. L. G.; Parker, D. H. Photophysics of O_2 excited by tunable laser radiation around 193 nm. *J. Chem. Phys.* **2000**, *112*, 4037−4044.

(10) Buijsse, B. Dissociation of Atmospheric Diatomic Molecules: Oxygen and Nitrogen. Ph.D. Thesis, University of Nijmegen, 1998.

(11) Herzberg, G. *Molecular Spectra and Molecular Structure, Spectra of Diatomic Molecules*; Van Nostrand Reinhold Co.: New York, 1950.

(12) Slater, J. C. *Quantum Theory of Molecules and Solids, I, Electronic Structure of Molecules*; McGraw-Hill: New York, 1953.

(13) Solomon, J. Photodissociation as studied by Photolysis Mapping. *J. Chem. Phys.* **1967**, *47*, 889−895.

(14) Taniguchi, N.; Takahashi, K. I.; Matsumi, Y.; Dylewski, S. M.; Geiser, J. D.; Houston, P. L. Determination of the heat of formation of O_3 using vacuum ultraviolet laser-induced fluorescence spectroscopy and two-dimensional product imaging techniques. *J. Chem. Phys.* **1999**, *111,* 6350−6355.

(15) Heck, A. J. R.; Chandler, D. W. Imaging Techniques for the Study of Chemical Reaction Dynamics. *Annu. Rev. Phys. Chem.* **1995**, *46,* 335−372.

(16) Tonokura, K.; Schafer, N.; Matsumi, Y.; Kawasaki, M. Photodissociation of oxygen molecules at 226 nm in the Herzberg I Continuum. *J. Chem. Phys.* **1991**, *95,* 3394−3398.

(17) Singer, S. J.; Freed, K. F.; Band, Y. B. Cross sections and angular distributions for individual fragment fine structure levels produced in one- and two-photon photodissociation of NaH. *J. Chem. Phys.* **1984**, *81*, 3091−3101.

(18) Huang, Y.-L.; Gordon, R. J. The multiplet state distribution of $O(^3P_J)$ produced in the photodissociation of O_2 at 157 nm. *J. Chem. Phys.* **1991**, *94*, 2640−2647.

(19) Leahy, D. J.; Cyr, D. R.; Osborn, D. L.; Neumark, D. M. Predissociation dynamics of the O_2 $B^3\Sigma_u^-$ state: Vibrational state dependence of the product fine-structure distribution. *J. Chem. Phys.* **1995**, *103*, 2495−2508.

(20) Lewis, B. R.; Gibson, S. T.; Dooley**,** P. M. Fine-structure dependence of predissociation linewidth in the Schumann−Runge bands of molecular oxygen. *J. Chem. Phys.* **1994**, *100* 7012−7035.

(21) Lin, J. J.; Hwang, D. W.; Lee, Y. T., Yang, X. Photodissociation of O_2 at 157 nm: Experimental Observation of anisotropy mixing in the $O_2 + h\nu \rightarrow O(^3P) + O(^3P)$ channel. *J. Chem. Phys.* **1998**, *109,* 1758−1762 and references therein.

(22) Eppink, A. T. J. B.; Parker, D. H.; Janssen, M. H. M.; Buijsse, B.; van der Zande, W. J. Production of Highly Aligned $O(^1D)$ atoms from Two-step Photodissociation of Molecular Oxygen. *J. Chem. Phys* **1998**, *108,* 1305−1308.

(23) Lewis, B. R.; Gibson, S. T.; Slanger T. G.; and Heustis**,** D. L. The $B^3\Sigma_u^- \leftarrow b^1\Sigma_g^+$ transition of molecular oxygen. *J. Chem. Phys.* **1999**, *110,* 11129−11132.

(24) Stephens, J. A.; Braunstein, M.; McKoy, V. Shape-resonance-induced non-Franck−Condon effects in the (2 + 1) resonance enhanced multiphoton ionization of the $C^3\Pi_g$ state of O_2. *J. Chem. Phys.* **1988**, *89*, 3923−3925.

(25) Wang, L.; Kohguchi, H.; Suzuki, T. Femtosecond time-resolved photoelectron imaging. *Faraday Discuss.* **1999**, *113*, 37−46.

AR980012D